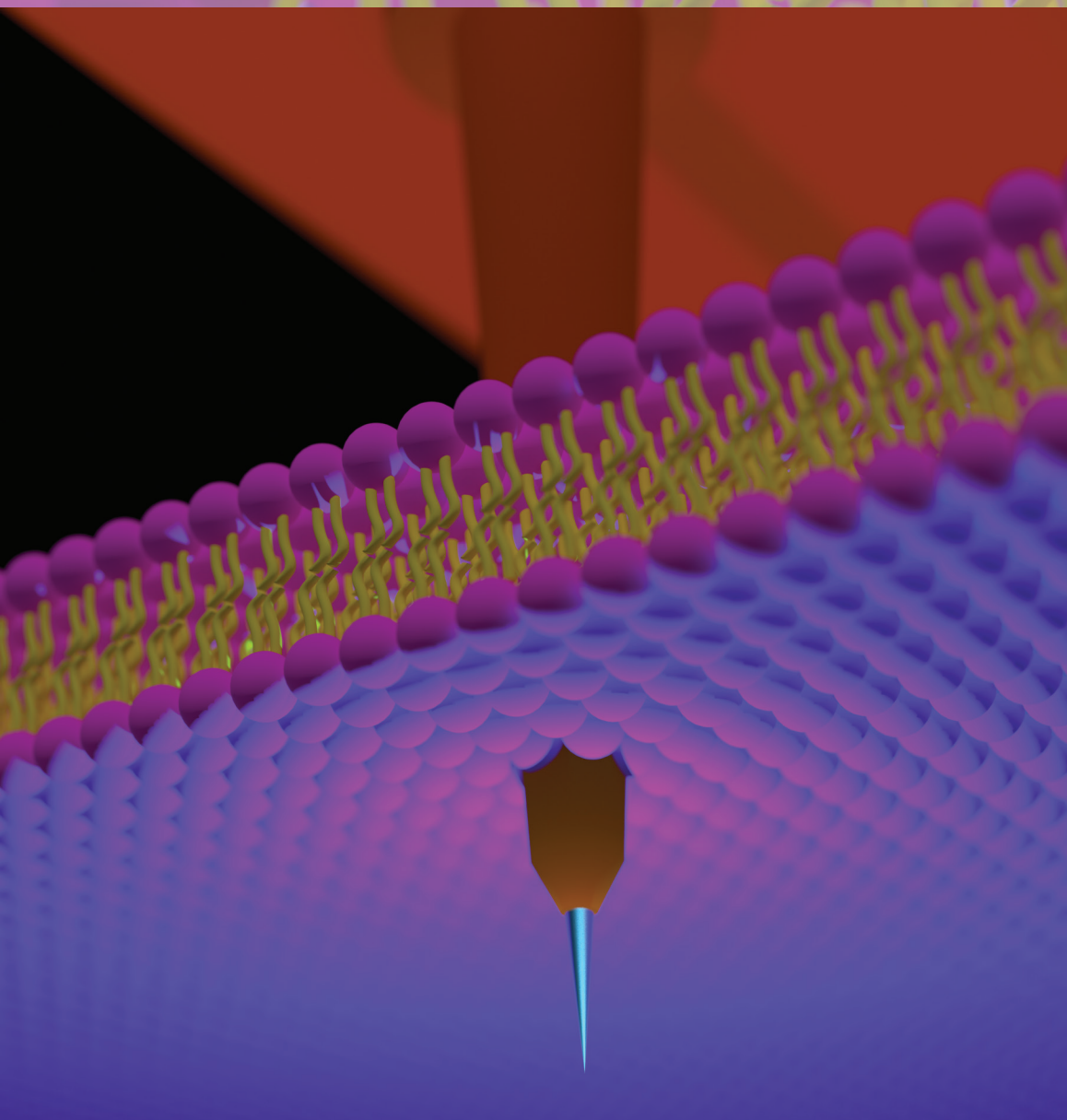


NANO MICRO

small

www.small-journal.com



21/2016

WILEY-VCH

**Nanoscale-Tipped High-Aspect-Ratio Vertical Microneedle
Electrodes for Intracellular Recordings**

T. Kawano and co-workers

Nanoscale-Tipped High-Aspect-Ratio Vertical Microneedle Electrodes for Intracellular Recordings

Yoshihiro Kubota, Hideo Oi, Hirohito Sawahata, Akihiro Goryu, Yoriko Ando, Rika Numano, Makoto Ishida, and Takeshi Kawano*

Micro/nanoscale diameter electrode devices have contributed significantly to the electrophysiological studies on neuron communications in brain tissue. One especially powerful methodology is intracellular recording, which provides recorded neuronal signals with a large amplitude (≈ 100 mV) and signal quality (excitatory and inhibitory postsynaptic potentials) compared to extracellular recording, which produces attenuated intracellular signals (< 100 μ V signal amplitude and without postsynaptic potentials).^[1,2] Nanowire- and nanotube-based nanoscale electrode devices used in the intracellular recordings demonstrate the important advantages of low-invasive,^[3-5] high-spatial-resolution, and high signal-to-noise (S/N) ratio.^[6-11] Spira et al. have reviewed the features of nanowire- and nanotube-based nanoscale electrode devices for intracellular applications.^[1] However, applications to biological tissue samples (e.g., brain slices and brain in vivo) are limited due to the tissue-penetrating nanoelectrode portions with lengths < 10 μ m. Table S1 (Supporting Information) compares the geometric features. Geometrical issues of these nanoelectrodes include difficulties fabricating such high-aspect-ratio nanowire/tube electrodes and an insufficient stiffness of the nanowire/tube themselves to punch biological tissue.

The approach reported herein can address the geometrical limitations of nanoelectrodes. For extracellular recording applications, we have previously fabricated microscale diameter high-aspect-ratio needle arrays by vapor-liquid-solid

(VLS) growth of silicon microneedles (7 μ m diameter needle tip and 210 μ m needle length) and demonstrated in vivo extracellular recordings using a rodent brain.^[12] The advantages of the VLS process to fabricate microneedles include precisely controlling the diameter and position of the needle as well as assembling a high-density array of microneedles. We have previously confirmed that the needle size minimizes tissue damage during needle penetration.^[12] In addition, these needles can be fully integrated with the metal oxide semiconductor (MOS) process.^[13-15]

To realize intracellular recordings, herein a nanoscale-tipped (< 1 μ m) microneedle electrode (NTE) (**Figure 1a**) is fabricated based on VLS grown silicon microneedles (> 100 μ m in length, $\langle 111 \rangle$ crystal growth direction, Supporting information)^[16-19] by sharpening the tip portion of the silicon microneedles (**Figure 1b**).^[20] As a step toward intracellular recording applications to neurons/cells in biological samples (e.g., brain slice and brain in vivo), we report the fabrication processes of the NTE as well as the electrical and mechanical properties of a > 100 μ m long NTE. Additionally, we demonstrate the intracellular recording capability using a tibialis anterior muscle of mouse.

To realize a powerful methodology of intracellular recordings within biological tissue samples, the needle electrode should be > 100 μ m in length, e.g., $>$ tens of micrometers for a brain slice and > 200 μ m for II–III layers in rodent's brain in vivo.^[21] Such intracellular recordings of the postsynaptic potentials from neurons within a brain tissue should help elucidate individual neurons and the circuit behavior.^[1] However, the stiffness of > 100 μ m long nanoscale diameter needles (e.g., silicon) is insufficient to punch a biological tissue, causing the needle to buckle and/or break prior to tissue penetration.^[22]

To achieve an intracellular electrode for biological tissue samples, the reported approach forms a cone-like-shaped long needle electrode with a nanoscale tip (**Figure 1b**). **Figure 1c** quantitatively compares the bending stiffness between cylindrical (diameter = 500 nm, length = 150 μ m) and cone-like (tip diameter = 500 nm, base diameter = 10 μ m, length = 150 μ m) needles of silicon (silicon needle by VLS growth method, Young's modulus = 188 GPa for $\langle 111 \rangle$) when applying a force (10 nN shown in **Figure 1c**). The cone-like needle exhibits a needle stiffness of 4.09 N m⁻¹, which is ≈ 7500 times higher than a cylindrical needle's stiffness (5.2×10^{-4} N m⁻¹). We have demonstrated the in vivo and in

Y. Kubota, Prof. H. Sawahata, Dr. A. Goryu,
Prof. M. Ishida, Prof. T. Kawano
Department of Electrical and Electronic
Information Engineering
Toyohashi University of Technology
1-1, Hibiyaoka, Tempaku-cho,
Toyohashi 441-8580, Japan
E-mail: kawano@ee.tut.ac.jp

Prof. H. Oi, Dr. Y. Ando, Prof. R. Numano, Prof. M. Ishida
Electronics-Inspired Interdisciplinary Research Institute (EIIRIS)
Toyohashi University of Technology
1-1, Hibiyaoka, Tempaku-cho, Toyohashi 441-8580, Japan
Prof. R. Numano
Department of Environmental and Life Science Engineering
Toyohashi University of Technology
1-1, Hibiyaoka, Tempaku-cho, Toyohashi 441-8580, Japan

DOI: 10.1002/sml.201600172



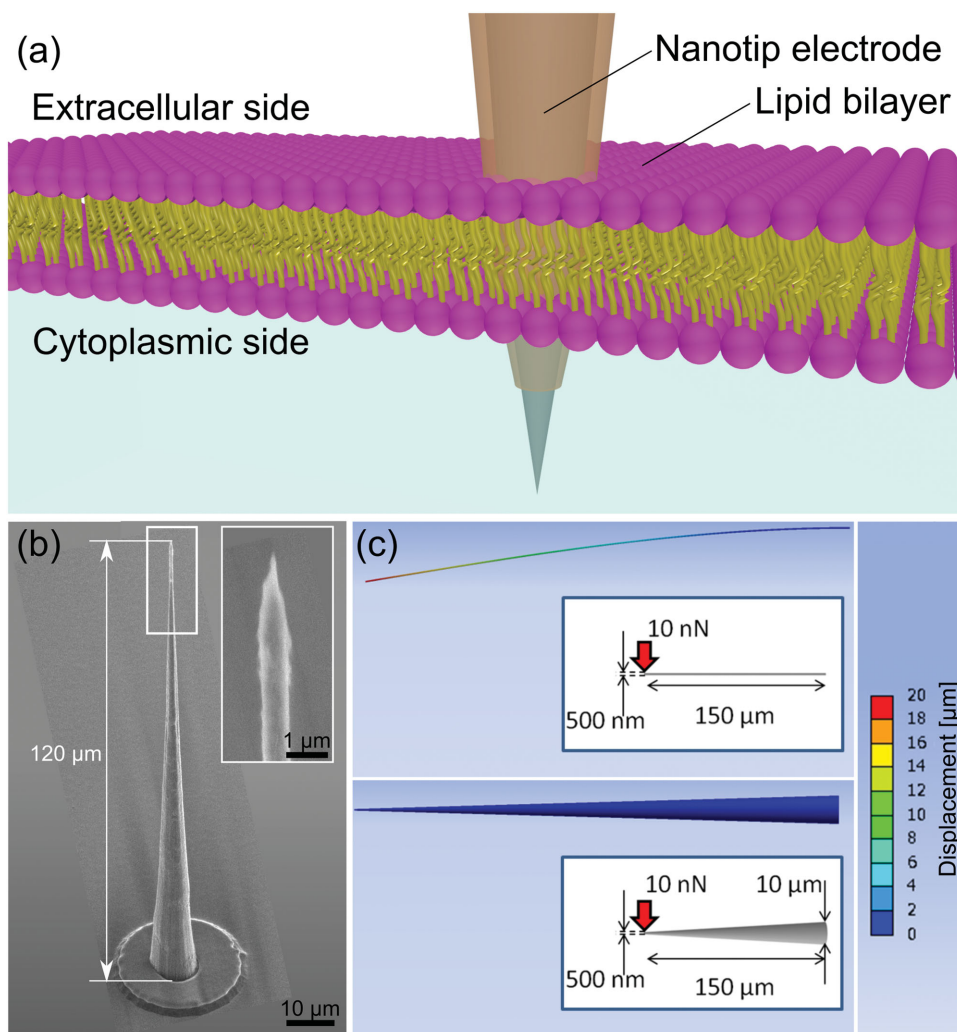


Figure 1. Intracellular recording using a high-aspect-ratio nanoscale-tipped electrode (NTE). a) Schematic showing a nanoelectrode punching a cell membrane. b) SEM image showing a nanoscale-tip, microscale-base, cone-like-shaped long silicon-needle fabricated by vapor-liquid-solid (VLS) growth of silicon microneedle followed by the nanoscale tip formation. The tip and base diameters of the needle are 500 nm and 10 μm , respectively, and the needle length is 120 μm . c) Schematics and simulation results of bending cylindrical and cone-like silicon needles upon applying force. Diameter and height of the cylindrical needle are 500 nm and 150 μm , respectively, while the cone-like needle has the same height but has a tip diameter of 500 nm and a 10 μm diameter at the base (Young's modulus = 188 GPa for (111) silicon needle, 10 nN for applied force). Color scale denotes displacement of the bent needle.

vitro brain tissue penetrations of 260 μm thick silk film supported 650 μm long silicon microneedles^[19] with a calculated needle stiffness of $2.91 \times 10^{-1} \text{ N m}^{-1}$. These results suggest that the cone-like needle enhances the needle's stiffness to punch a biological tissue and realize intracellular recordings within the tissue.

The fabrication process of the NTE is based on VLS growth of vertical high-aspect-ratio silicon microneedles, subsequent nanoscale tip formation, and micro/nanofabrication processes.^[20,23] A silicon-on-insulator (SOI) substrate, consisting of a 2 μm thick (111)-top-silicon (n-type with a resistivity of $<0.02 \Omega \text{ cm}$)/4 μm thick buried oxide layer/525 μm thick (111)-silicon substrate (n-type with a resistivity of $<0.02 \Omega \text{ cm}$), was used to fabricate the NTE (Figure 2a). To form the silicon platform for VLS growth of the silicon needle, a silicon island was patterned with the (111)-top-silicon layer (Figure 2b). The islands were

subsequently covered with an insulating layer of silicon dioxide by wet oxidation (Figure 2c). The silicon dioxide film was then exposed, where a catalytic gold used for VLS growth was placed by evaporation and lift-off (Figure 2d). With a 200 nm thick, 6 μm diameter gold catalyst, a vertical 140 μm long silicon microneedle with an $\approx 10 \mu\text{m}$ diameter at the base was formed by VLS growth of silicon (Figure 2e).^[18,24] Silicon chemical etching at the tip section of the microneedle with the etching solution (HF, HNO₃, and H₂O) prepared the $<500 \text{ nm}$ tipped silicon microneedle^[20,25] (Figure 2f). The angle controllability of the nanotip was confirmed by changing the ratio of the etching solution and the etching time.^[20]

Both needle metallization and device interconnection were conducted by iridium sputtering with a binding layer of titanium (total thickness of iridium/titanium multilayer = 200 nm) (Figure 2g). Iridium is used as the

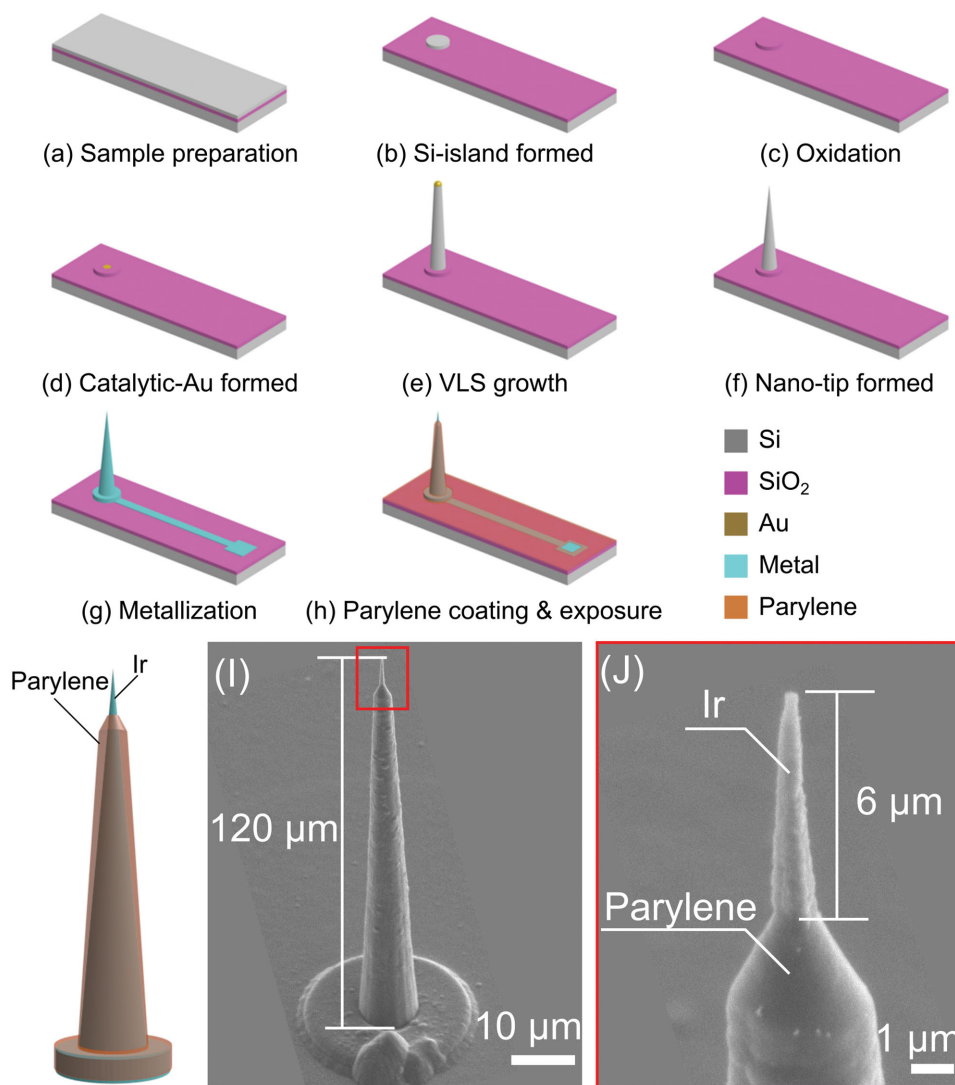


Figure 2. Fabrication of an NTE device. a,b) Silicon-island formation with a (111)-top-silicon layer of silicon-on-insulator substrate, c) wet oxidation of the island, d) etching of silicon-dioxide and catalytic gold formation on the silicon island by evaporation and lift-off, e) vapor–liquid–solid growth of the silicon microneedle, f) formation of nanoscale-tipped silicon microneedle by silicon chemical etching, g) metallization of the needle and interconnection with iridium (titanium is used as the binding layer), and h) needle encapsulation with parylene-C, and exposure of the iridium tip and bonding pad from the parylene layer by oxygen plasma. i,j) SEM images of a fabricated NTE device. The tip and base diameters of the NTE are <300 nm and $10\ \mu\text{m}$, respectively, with a length of $120\ \mu\text{m}$. Height of the iridium nanotip exposed from the parylene shell is $\approx 6\ \mu\text{m}$ ($\approx 9.5\ \mu\text{m}^2$ for area).

recording electrode site because it has a low electrical impedance characteristic in saline.^[26,27] The metallized nanotip of the needle exhibits a diameter <300 nm and a tip curvature radius of <200 nm. After device metallization, the sidewall of the iridium needle and the device interconnection were insulated by forming a $<1\ \mu\text{m}$ thick biocompatible layer of parylene-C (Figure 2h). The parylene shelled needle was then coated with a spray-coated photoresist for subsequent tip exposure.

Oxygen plasma with a $0.3\ \mu\text{m}\ \text{min}^{-1}$ photoresist etching rate was used to expose the recording site of the nanotip, realizing a controlled height/area of the iridium nanotip exposed from the parylene shell. Herein the height of the nanotip is $\approx 6\ \mu\text{m}$ ($\approx 9.5\ \mu\text{m}^2$ for area, the iridium area represents an electrode impedance of $1\text{--}5\ \text{M}\Omega$ at $1\ \text{kHz}$ in saline^[26]). The length of the fabricated NTE is $120\ \mu\text{m}$ (Figure 2i,j), which is suitable for biological tissues, including brain slices.

The electrolyte/metal interfacial impedance of the electrode is an important characteristic of an intracellular electrode. **Figure 3a** is the equivalent circuit of an individual NTE, consisting of an electrode impedance (Z_e) and a parasitic impedance associated with the interconnection (Z_1). The electrode impedance Z_e was experimentally obtained by measuring the total impedance ($Z_e//Z_1$) and subtracting the interconnection impedance Z_1 from the $Z_e//Z_1$.

Figure 3b shows the impedances of $Z_e//Z_1$ taken from the three NTEs (#1, 2, and 3). NTEs #1, 2, and 3, which were measured in a room temperature phosphate buffered saline (PBS) bath, exhibit $Z_e//Z_1$ impedances from $823\ \text{M}\Omega$ to $235\ \text{k}\Omega$ at a frequency range of $1\ \text{Hz}\text{--}10\ \text{kHz}$ (Figure 3b). Because the designed value of the interconnection impedance Z_1 is $10.2\ \text{G}\Omega\text{--}1.02\ \text{M}\Omega$ at $1\ \text{Hz}\text{--}10\ \text{kHz}$ (Figures S1 and S2, Supporting Information), the electrode impedances Z_e for

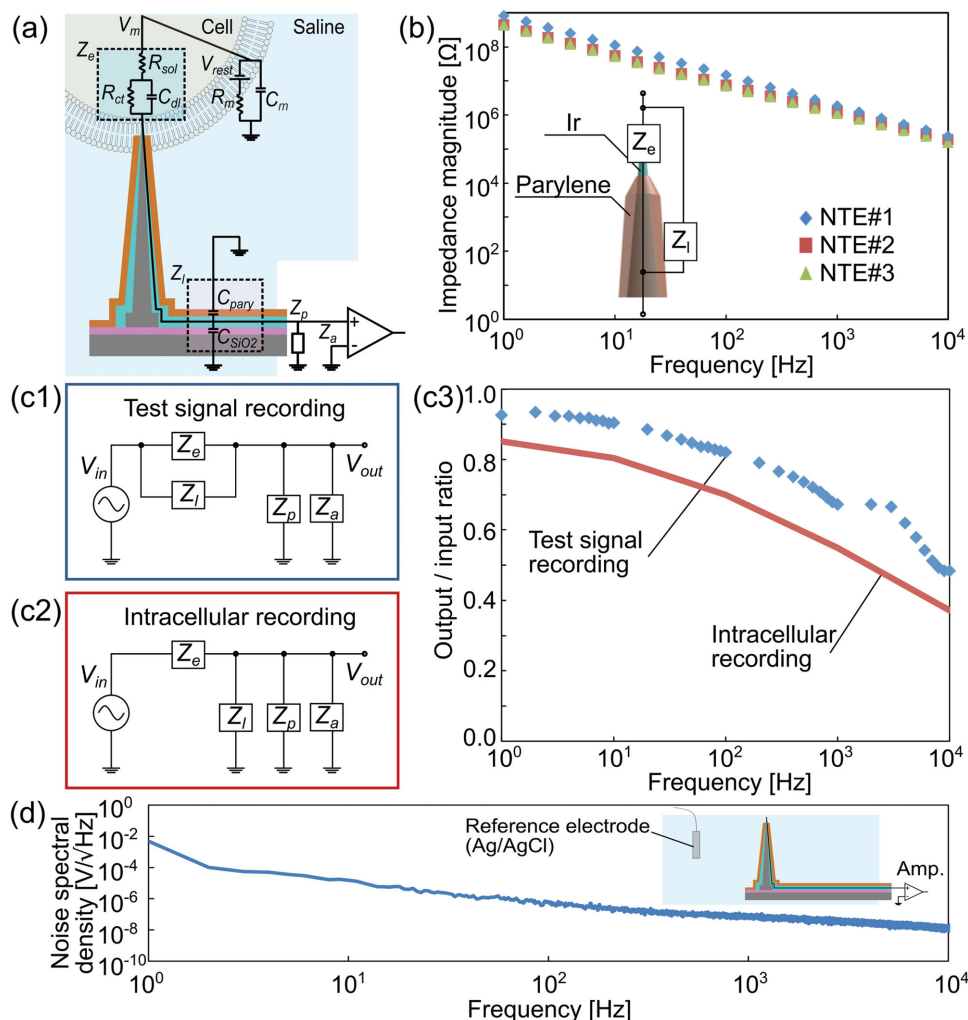


Figure 3. Electrical characteristics of a fabricated NTE device. a) Equivalent circuit model of an individual NTE device. Electrolyte/metal interfacial impedance (Z_e) consists of resistances of solution (R_{sol}), charge transfer (R_{ct}), and double-layer capacitance (C_{dl}). Parasitic impedance associated with the device interconnection (Z_i) consists of capacitances of parylene (C_{par}) and silicon dioxide (C_{SiO_2}). Other parasitic impedances from the recording cable to the amplifier are cable impedance (Z_p) and input impedance of amplifier (Z_a). Cell consists of membrane capacitance (C_m), membrane resistance (R_m), membrane resting potential (V_{rest}), and potential due to these elements (V_m). b) Magnitude of the electrical impedances (Z) of the three NTEs (NTEs #1, #2, and #3) measured in room-temperature phosphate-buffered saline. c) Equivalent circuit models for the test-signal recording (c1) and intracellular recording (c2) of the recording system, and graph showing the output/input signal amplitude ratios taken from the test-signal recording measured in room-temperature phosphate-buffered saline upon applying 2 mV_{pp} sinusoidal test signals (c3). Graph also includes the calculated output/input signal amplitude ratios for intracellular recording by considering the grounded interconnection impedance (Z_i) in an actual intracellular recording. d) Noise of the recording system. Herein the NTE device is immersed in a room-temperature Ringer's solution bath grounded with a reference electrode of silver–silver chloride. Ringer's solution bath and reference electrode are consistent with that used in the intracellular recording (Figure 4).

NTE #1 at the frequency range are 895 MΩ–305 kΩ (Z_e at 1 kHz for an action potential recording application is 2.3 MΩ). By considering Z_i , the electrode impedances of NTEs #2 and #3 at 1 Hz–10 kHz are 461 MΩ–230 kΩ and 445 MΩ–186 kΩ, respectively. These impedances are similar to those of conventional intracellular metal electrodes and glass pipettes.^[1]

The output/input (O/I) signal amplitude ratio of the fabricated NTE device in PBS was also measured by applying input test signals (sinusoidal waves with 2 mV_{pp} amplitude) to the PBS bath. Figure 3c shows the O/I ratios of NTE #1 at 1 Hz–10 kHz (data not shown for NTEs #2 and #3). Because the impedances of Z_e and Z_i result in the low-pass

characteristics of the recording system,^[12,28] the O/I ratio decreases as the frequency increases. During the test signal recording, the O/I ratio at 1 kHz is ≈70% (“Test signal recording” in Figure 3c). The ratio decreases due to the grounded interconnection impedance (Z_i) in an actual neural recording^[12,28] (“Intracellular recording” in Figure 3c). By considering the grounded Z_i (10.2 GΩ–1.02 MΩ at 1 Hz–10 kHz), the O/I ratios of the recording system in neural recording are 85%–37% at 1 Hz–10 kHz. Because the measured noise of the recording system is 5 mV Hz^{-1/2}–15 nV Hz^{-1/2} at 1 Hz–10 kHz (Figure 3d), 85%–37% of the attenuated intracellular potentials of ≈100 mV can be obtained with a high S/N ratio using the fabricated NTE device.

The intracellular recording capability of the fabricated NTE devices was verified by measuring the resting membrane potentials of mouse's tibialis anterior muscle cells. A total of 14 NTEs were used in the penetrations using seven tibialis anterior muscles. Herein the tibialis anterior muscle was extracted from a deeply anesthetized mouse (adult mouse, >20 g weight) with urethane (50 μL of 30% solution/10 g body weight). The muscle was immersed in a room temperature Ringer's solution bath (NaCl: 8.6 g L^{-1} , KCl: 0.3 g L^{-1} , $\text{CaCl}_2 \cdot 2\text{H}_2\text{O}$: 0.33 g L^{-1}). The fabricated NTE device was packaged with a polyimide flexible printed circuit cable, which was connected to a recording amplifier (input impedance: $10^{10} \Omega$, gain: 1, with offset output voltage control). The signals recorded through the amplifier were acquired with a digital signal-processing module. **Figure 4a** shows the measurement system used in the intracellular recordings. The NTE device, which was mounted on an *xyz* manipulator, was

positioned over the muscle cells with the electrode side facing down, and then the electrode penetrated the muscle cell.

Once the NTE penetrated into the muscle cell, potential changes between the un-penetrated and the penetrated NTE are observed. **Figure 4b** shows microscope observations before and after NTE penetration into a muscle cell (Movie S1, Supporting Information). **Figure 4c** shows the simultaneously measured potential changes associated with the NTE penetrations; top (**Figure 4c1**), middle (**Figure 4c2**), and bottom (**Figure 4c3**) waveforms were individually obtained via the NTE #1, #2, and #3 (electrical properties shown in **Figure 3b**), respectively. Such potential changes associated with NTE penetrations were also detected via two other NTEs (electrode impedances at 1 kHz were 1.8 and 2.8 M Ω , respectively) (**Figure S5**, Supporting Information); 5 of the 14 penetrated NTEs detected the potential changes. The measured potential changes are ≈ -35 mV (NTE #1,

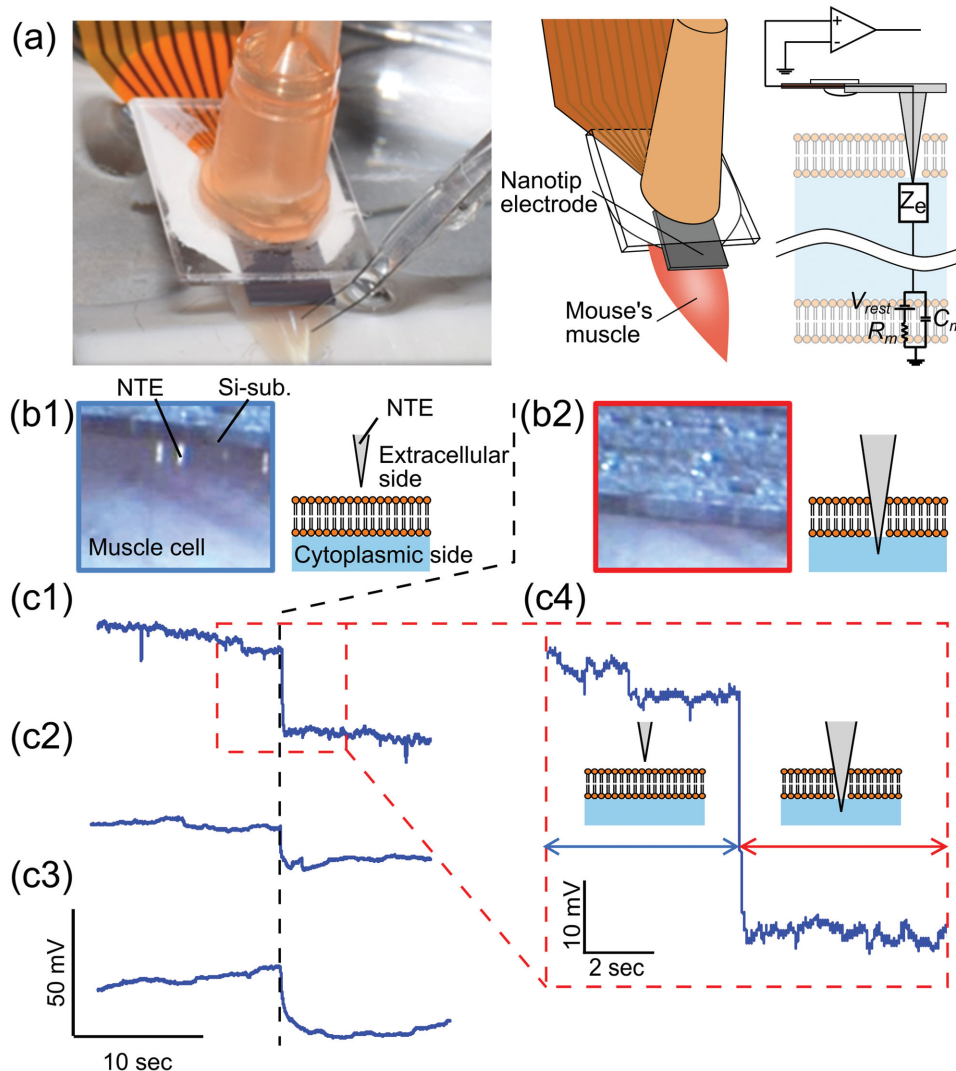


Figure 4. Intracellular recordings via fabricated NTEs. a) Photograph and schematic of the measurement system. Fabricated NTE device packaged with a flexible cable is mounted on an *xyz* manipulator and positioned over and penetrated into a mouse's tibialis anterior muscle. b) Schematics and photograph of b1) un-penetrated and b2) penetrated NTE into the muscle cell. c) Observed potential changes associated with the NTE penetrations. c1) Top, c2) middle, and c3) bottom waveforms are individually obtained via NTE #1, #2, and #3, respectively (the impedance characteristics are shown in **Figure 3b**). c4) Enlarged waveform is taken from the top waveform of the measured potential via c1) NTE #1. Note that the data are low-pass filtered (bandpass: DC – 100 Hz).

Figure 4c 1), ≈ -19 mV (NTE #2, Figure 4c 2), and ≈ -30 mV (NTE #3, Figure 4c3). Although the potential changes vary with the used NTEs, the timings of the potential changes are consistent with that of NTE penetration, which was confirmed by microscope observations (Figure 4b). We also verified that a conventional glass pipette detects the resting membrane potentials of the muscle cells with the amplitude of ≈ -56 mV using the same recording and data acquisition systems (Figure S3, Supporting Information). Moreover, to support the results of the iridium-NTEs (Figure 4), we further investigated the intracellular recording capability using another NTE with a different electrode material of aluminum (120 μm long needle, 7 μm height aluminum-nanotip, Figure S6, Supporting Information). Aluminum, which reacts with chloride ions, shows the potential changes using different concentrations of chloride ions in solution during the electrochemical measurements. Due to the difference in concentration of the chloride ions between the extracellular Ringer's solution (155.7 mmol L^{-1} for chloride ions) and the intracellular fluid (a lower chloride ion concentration of 4 mmol L^{-1} [29]), the aluminum-NTE in the Ringer's solution before the muscle cell penetration shows the chloride reaction-induced noisy and drift characteristics. These characteristics are reduced after penetration (Figure S6, Supporting Information), indicating the aluminum-NTE penetrates into the cell. In addition, the intracellular potential-induced potential changes are repetitively observed before and after the cell penetrations (Figure S6, Supporting Information). These results suggest that the NTEs penetrate the muscle cell with a sufficient needle stiffness and detect the resting membrane potentials (intracellular potentials) of the cell.

Electrical impedance, O/I signal amplitude ratio, and noise characteristics of the fabricated NTE are dominated by the height/area of the iridium tip section. In this study, the height and area of the iridium tip exposed from the parylene shell are ≈ 6 μm and ≈ 9.5 μm^2 , respectively. Oxygen plasma with an etching rate of 0.3 $\mu\text{m min}^{-1}$ exposed the tip (Figure S4, Supporting Information). The plasma process shows an etching uniformity and is suitable for batch exposure of the NTE tips. Increasing the exposed height/area of the iridium tip reduces the electrical impedance while simultaneously increasing the O/I ratio of the recording system.^[12] However, an insufficient penetration of a longer iridium tip section (>6 μm in height) into the cell may cause that the iridium tip is in contact with the extracellular Ringer's solution. This induces the electrical leakage between the inside (cytoplasmic side) and outside (extracellular side) of the cell, decreasing the changes in the resting potential (Figure 4c). Without increasing the height/area of the iridium nanotip site, one way to improve the electrical properties of the NTE and the recording system is to use a low impedance material, as discussed later.

The fabricated NTEs measured the resting membrane potentials of mouse's muscle cell with an amplitude of ≈ -19 to ≈ -35 mV. The potential changes due to the resting potential are smaller than that of the potential changes measured via a glass pipette (≈ -56 mV, see Figure S3, Supporting Information). As mentioned, such attenuation of the potential changes are probably due to the insufficient insertion of the NTE into the cell. Because the electrode tip has ≈ 6 μm

height, an insufficient electrode penetration results in electrical contact with the extracellular Ringer's solution. This induces electrical leakage between the inside (cytoplasmic side) and the outside (extracellular side) of the cell, attenuating the measured resting potential. In addition, the muscles itself degrade as the recording time increases. Herein, the recording time exceeded 40 min, while the muscle was penetrated with NTEs and glass pipettes repetitively.

The fabricated NTEs can be repetitively inserted and extracted from the muscle cell without breaking the NTE (Movie S1, Supporting Information). Although the length of the fabricated NTE exceeds 120 μm , the NTE does not buckle and exhibits a sufficient stiffness to punch the cell during the penetrations, enabling the intracellular recording. Due to the cone-like shape of the NTE (tip diameter < 500 nm, base diameter = 10 μm), the NTE stiffness is higher than that of the cylindrical-shaped silicon needle with the same length and tip diameter, as quantitatively confirmed in the bending simulations (Figure 1c). In addition, penetration capability of the nanotip silicon microneedle has been confirmed using a brain tissue phantom of gelatin (6.5 wt% in water).^[20,23]

The NTE with the length of >100 μm is applicable to biological samples including brain slice and brain in vivo. Tissue damage associated with the needle penetration is due to two reasons: needle size and needle flexibility. The needle portion of the fabricated NTE has the diameter of <10 μm , which small needle size minimizes tissue damage as demonstrated in our previous work on immunohistochemical analysis using a rat brain.^[12] Although silicon is a stiffer material (188 GPa Young's modulus for $\langle 111 \rangle$ silicon) than other flexible needle materials (e.g., polymer), the decreased diameter of the silicon needle increases the needle's flexibility (needle's flexibility is proportional to $1/r^4$, where r is radius of the needle).^[12] We have also confirmed the silicon needle's flexibility and the absence of fragile properties using both needle bending tests and in vivo animal experiments.^[12,19]

In the future, the NTE signal quality of the intracellular recording should be improved. One way to enhance the signal quality of the recording system is to reduce the electrical impedance of the NTE. As previously mentioned, increasing the exposed height/area of the iridium tip reduces the impedance while simultaneously increasing the O/I ratio of the recording system.^[12] Without increasing the height/area of the iridium nanotip site, the electrical properties of the NTE and the recording system can be improved by using a low impedance material as the nanotip recording site. Candidate materials include iridium oxide^[26,30] and poly(3,4-ethylenedioxythiophene) (PEDOT),^[27,31–33] which have lower impedance characteristics than iridium. While recording, it is also necessary to reduce the potential drift (Figure 4c), which is due to the electrical characteristics of the electrolyte-metal (iridium) electrode interface. The recording system has a measured potential drift of ≈ 50 mV min^{-1} . Correcting the potential drift is crucial to achieve stable intracellular recordings using a nanoscale metal electrode. This potential drift can be improved by using the same material for both the recording and reference electrodes because the effect of charged electrodes is eliminated. Moreover, employing a material with a low junction potential characteristic, such as

silver–silver chloride, should improve the electrical properties of the electrolyte/electrode interface.

Increasing the stiffness of the high-aspect-ratio nano-electrode enhances the recording applications not only for cultured neurons/cells but also for neurons/cells within biological tissue samples, including brain slices and brain in vivo. Because the diameter of the needle base further increases with vapor-phase silicon film deposition in VLS growth,^[24,34,35] numerous base diameters for longer NTEs (>120 μm) with a sufficient stiffness can be formed without increasing the tip diameter, realizing intracellular recordings for deep cell layers in brain tissues, e.g., ≈100–1300 μm for II–VI layers in rodent's brain.^[21]

Although we demonstrated the recording capability of the fabricated NTEs by measuring the resting membrane potential of a muscle cell, an NTE device with the aforementioned electrical properties (a frequency range of 1 Hz–10 kHz, Figure 3) can record the intracellular action potentials (≈1 kHz). Herein the action potential recording of a muscle cell via the NTE was limited because we did not want to break the needle portion of the NTE device due to the movements of the muscle itself. To eliminate the movements of the muscle, a methodology such as a calcium channel blocker for the target cell can be used. As a step toward multichannel intracellular action potential recordings of deep cell layers in a tissue (>≈100 μm depth for brain slices and brain in vivo), we are currently fabricating an array of NTEs.

Micro/nanofabrication processes realize <300 nm tip diameter, 120 μm long microneedle electrode devices for intracellular recording applications. We demonstrated the capability of the intracellular electrodes using a tibialis anterior muscle of mouse. Batch fabrication and integration of such >100 μm long needle intracellular electrodes should advance device technologies and eventually realize multisite-, depth-intracellular recordings for biological tissues, including brain slices and brain in vivo, which are beyond the capability of conventional devices.

Experimental Section

Animal Experiments: All experimental procedures using mice and animal care were approved by the animal experiments committee of Toyohashi University of Technology.

Data Acquisition and Signal Processing for the Intracellular Recording: The fabricated NTE device, which was packaged with a polyimide flexible printed circuit cable, was connected to a recording amplifier (input impedance of 10¹⁰ Ω and a gain of 1 with offset output voltage control). The signals through the recording amplifier were acquired with a digital signal processing module (RZ2, Tucker-Davis Technologies). Digital data were acquired using a hard disk in a Windows PC. The data in intracellular recordings (Figure 4c) were low-pass filtered (DC – 100 Hz).

Supporting Information

Supporting Information is available from the Wiley Online Library or from the author.

Acknowledgements

This work was supported by Grants-in-Aid for Scientific Research (S) (No. 20226010), (A) (No. 25249047), for Young Scientist (A) (No. 26709024), (B) (No. 22760251), and the PRESTO Program from JST. Y.K. was supported by the Leading Graduate School Program R03 of MEXT. R.N. was also supported by a Grant-in-Aid for Scientific Research (C) (No. 24590350), the Asahi Glass Foundation, and the Takeda Science Foundation.

- [1] M. E. Spira, A. Hai, *Nat. Nanotechnol.* **2013**, *8*, 83.
- [2] E. Chorev, J. Epshtein, A. R. Houweling, A. K. Lee, M. Brecht, *Curr. Opin. Neurobiol.* **2009**, *19*, 513.
- [3] R. Singhal, Z. Orynbayeva, R. V. K. Sundaram, J. J. Niu, S. Bhattacharyya, E. A. Vitol, M. G. Schrlau, E. S. Papazoglou, G. Friedman, Y. Gogotsi, *Nat. Nanotechnol.* **2011**, *6*, 57.
- [4] S.-W. Han, C. Nakamura, N. Kotobuki, I. Obataya, H. Ohgushi, T. Nagamune, J. Miyake, *Nanomedicine* **2008**, *4*, 215.
- [5] A. K. Shalek, J. T. Robinson, E. S. Karp, J. S. Lee, D.-R. Ahn, M.-H. Yoon, A. Sutton, M. Jorgolli, R. S. Gertner, T. S. Gujral, G. MacBeath, E. G. Yang, H. Park, *Proc. Natl. Acad. Sci. USA* **2010**, *107*, 1870.
- [6] R. Gao, S. Strehle, B. Tian, T. Cohen-Karni, P. Xie, X. Duan, Q. Qing, C. M. Lieber, *Nano Lett.* **2012**, *12*, 3329.
- [7] C. Xie, Z. Lin, L. Hanson, Y. Cui, B. Cui, *Nat. Nanotechnol.* **2012**, *29*, 997.
- [8] X. Duan, R. Gao, P. Xie, T. Cohen-Karni, Q. Qing, H. S. Choe, B. Tian, X. Jiang, C. M. Lieber, *Nat. Nanotechnol.* **2011**, *7*, 174.
- [9] J. T. Robinson, M. Jorgolli, A. K. Shalek, M.-H. Yoon, R. S. Gertner, H. Park, *Nat. Nanotechnol.* **2012**, *7*, 180.
- [10] B. Tian, T. Cohen-Karni, Q. Qing, X. Duan, P. Xie, C. M. Lieber, *Science* **2010**, *329*, 830.
- [11] Q. Qing, Z. Jiang, L. Xu, R. Gao, L. Q. Mai, C. M. Lieber, *Nat. Nanotechnol.* **2014**, *9*, 142.
- [12] A. Fujishiro, H. Kaneko, T. Kawashima, M. Ishida, T. Kawano, *Sci. Rep.* **2014**, *4*, 4868.
- [13] T. Kawano, Y. Kato, R. Tani, H. Takao, K. Sawada, M. Ishida, *IEEE Trans. Electron Devices* **2004**, *51*, 415.
- [14] K. Takei, T. Kawashima, T. Kawano, H. Takao, K. Sawada, M. Ishida, *J. Micromech. Microeng.* **2008**, *18*, 035033.
- [15] A. Okugawa, K. Mayumi, A. Ikedo, M. Ishida, T. Kawano, *IEEE Electron Device Lett.* **2011**, *32*, 683.
- [16] T. Kawano, H. Takao, K. Sawada, M. Ishida, *Jpn. J. Appl. Phys., Part 1* **2003**, *42*, 2473.
- [17] T. Kawano, T. Harimoto, A. Ishihara, K. Takei, T. Kawashima, S. Usui, M. Ishida, *Biosens. Bioelectron.* **2010**, *25*, 1809.
- [18] A. Ikedo, T. Kawashima, T. Kawano, M. Ishida, *Appl. Phys. Lett.* **2009**, *95*, 20.
- [19] S. Yagi, S. Yamagiwa, Y. Kubota, H. Sawahata, R. Numano, T. Imashioya, H. Oi, M. Ishida, T. Kawano, *Adv. Healthcare Mater.* **2015**, *4*, 1949.
- [20] A. Goryu, A. Ikedo, M. Ishida, T. Kawano, *Nanotechnology* **2010**, *21*, 125302.
- [21] J. Defelipe, *Front. Neuroanat.* **2011**, *5*, 29.
- [22] S. Hoffmann, I. Utke, B. Moser, J. Michler, S. H. Christiansen, V. Schmidt, S. Senz, P. Werner, *Nano Lett.* **2006**, *6*, 622.
- [23] A. Goryu, R. Numano, A. Ikedo, M. Ishida, T. Kawano, *Nanotechnology* **2012**, *23*, 415301.
- [24] T. Kawano, Y. Kato, M. Futagawa, H. Takao, K. Sawada, M. Ishida, *Sens. Actuators, A* **2002**, *97*, 709.
- [25] B. Schwartz, *J. Electrochem. Soc.* **1976**, *123*, 1903.
- [26] S. Yamagiwa, A. Fujishiro, H. Sawahata, R. Numano, M. Ishida, T. Kawano, *Sens. Actuators, B* **2015**, *206*, 205.
- [27] S. J. Wilks, S. M. Richardson-Burns, J. L. Hendricks, D. C. Martin, K. J. Otto, *Front. Neuroeng.* **2009**, *2*, 7.

- [28] T. Harimoto, K. Takei, T. Kawano, A. Ishihara, T. Kawashima, H. Kaneko, M. Ishida, S. Usui, *Biosens. Bioelectron.* **2011**, *26*, 2368.
- [29] H. Lodish, A. Berk, P. Matsudaira, C. A. Kaiser, M. Krieger, M. P. Scott, L. Zipursky, J. Darnell, *Molecular Cell Biology* W. H. Freeman, New York **2003**, p. 253.
- [30] S. F. Cogan, J. Ehrlich, T. D. Plante, A. Smirnov, D. B. Shire, M. Gingerich, J. F. Rizzo, *J. Biomed. Mater. Res., Part B* **2009**, *89*, 353.
- [31] D. Khodagholy, T. Doublet, M. Gurfinkel, P. Quilichini, E. Ismailova, P. Leleux, T. Herve, S. Sanaur, C. Bernard, G. G. Malliaras, *Adv. Mater.* **2011**, *23*, 268.
- [32] S. Venkatraman, J. Hendricks, Z. a. King, A. J. Sereno, S. Richardson-Burns, D. Martin, J. M. Carmena, *IEEE Trans. Neural Syst. Rehabil. Eng.* **2011**, *19*, 307.
- [33] M. R. Abidian, D. C. Martin, *Adv. Funct. Mater.* **2009**, *19*, 573.
- [34] R. S. Wagner, W. C. Ellis, *Trans. Metall. Soc. AIME* **1965**, *233*, 1053.
- [35] Y. Wang, V. Schmidt, S. Senz, U. Gösele, *Nat. Nanotechnol.* **2006**, *1*, 186.

Received: January 19, 2016

Revised: March 7, 2016

Published online: April 8, 2016